



## Full length article

## Effect of interstitial oxygen and nitrogen on incipient plasticity of NbTiZrHf high-entropy alloys

Y.X. Ye <sup>a,\*</sup>, B. Ouyang <sup>b,c</sup>, C.Z. Liu <sup>a</sup>, G.J. Duscher <sup>a</sup>, T.G. Nieh <sup>a,\*</sup><sup>a</sup> Department of Materials Science and Engineering, University of Tennessee, Knoxville, TN 37996, United States<sup>b</sup> Department of Materials Science and Engineering, University of California, Berkeley, Berkeley, CA, United States<sup>c</sup> Materials Science Division, Lawrence Berkeley National Laboratory, Berkeley, CA, United States

## ARTICLE INFO

## Article history:

Received 13 August 2020

Revised 24 August 2020

Accepted 25 August 2020

Available online 28 August 2020

## Keywords:

High-entropy alloys

Interstitials

Dislocation nucleation

Nanoindentation pop-in

Charge transfer

## ABSTRACT

In this work, instrumented nanoindentation was employed to investigate the effect of interstitial oxygen or nitrogen addition on the incipient plasticity and dislocation nucleation in a body-centered cubic NbTiZrHf high-entropy alloy (HEA) at loading rates of 10–1000  $\mu\text{N/s}$ . We conducted quantitative statistical analysis and density functional theory (DFT) calculations to identify the role of interstitial oxygen/nitrogen during the onset of plasticity. Synchrotron X-ray diffraction and transmission electron microscopy were also performed to confirm that the oxygen/nitrogen atoms were indeed present as interstitial solutes. These interstitial solutes could increase the critical shear stress required to initiate plasticity, and nitrogen yielded a larger hardening effect than oxygen. The activation volumes were evaluated to be about 2–3 atomic volumes, indicating cooperative migration of multiple atoms during the dislocation nucleation, and neither oxygen nor nitrogen appeared to significantly affect this activation process. Hardness tests were also carried out and the result demonstrated that the enhancement of the critical shear stress for incipient plasticity was not caused by the traditional solid-solution strengthening mechanism. DFT calculations revealed that oxygen/nitrogen interstitials induced local charge transfer and improved the lattice cohesion, which was probably responsible for the enhanced pop-in load/stress in the current interstitially alloyed HEAs.

Published by Elsevier Ltd on behalf of Acta Materialia Inc.

## 1. Introduction

Instrumented nanoindentation has been widely employed to probe the incipient plasticity in a variety of crystals [1–8]. Experimentally, the load-displacement curve is usually punctuated by a series of discrete displacement bursts, or pop-ins, which typically occurs at a shallow indentation depth in the order of nanometers. The first pop-in, designated as incipient plasticity, is generally controlled by dislocation nucleation triggered by a critical stress near the theoretical strength [1–8]. In the case of indenting stress-free surface of a well-annealed sample, which has a low dislocation density, the fine indenter tip has a high probability to impress into a sample volume that is completely absent of dislocation [9,10]. In addition, since the nucleation is a stochastic process, a large number of nanoindentation tests with nominally identical condition make it convenient to quantitatively assess the nucleation process based on the model combining transition state theory and Weibull statistics [1–3].

In the past decade, high-entropy alloys (HEAs), or multi-principal elements alloys (MPEAs), have drawn extensive research attention in the field of structural materials not only due to their attractive mechanical properties, such as high strength-ductility combination [11–13], excellent resistance to fracture [14], creep [15], and wear [16,17] etc., but also because this new class of materials expands the composition space for alloy design. Recently, a new category of HEAs, which contains interstitial elements, in light of interstitial solid-solution strengthening mechanism, have been emerged [11,18–20]. For example, Wang et al. [18] investigated the effect of interstitial carbon addition (up to 1.1 at.%) on mechanical properties and dislocation substructure evolution in a face-centered cubic (FCC)  $\text{Fe}_{40.4}\text{Ni}_{11.3}\text{Mn}_{34.8}\text{Al}_{7.5}\text{Cr}_6$  HEA. Another study also demonstrated that 0.5 at.-%nitrogen addition to an FCC NiCoCr medium entropy alloy (MEA) could increase its yield strength without losing the ductility [19]. It is especially noted that Lei et al. [11] have reported an extraordinary enhancement in both strength and ductility in an interstitial oxygen alloyed (2 at.%) body-centered cubic (BCC) NbTiZrHf HEA, surmounting the interstitial-induced embrittlement in conventional BCC alloys [21]. The ordered oxygen complexes formed in the alloy effectively pin

\* Corresponding authors.

E-mail addresses: [ye7@vols.utk.edu](mailto:ye7@vols.utk.edu) (Y.X. Ye), [tnieh@utk.edu](mailto:tnieh@utk.edu) (T.G. Nieh).

dislocations and promote their double cross-slip and multiplication during plastic deformation, thus simultaneously enhance the alloy's strength, work hardening capacity, and ductility.

It is noted that, in the study of interstitial-containing HEAs, the majority of published works focused on the effect of interstitial additions on the macroscopically plastic deformation during which the interstitial solutes act as obstacles to impede dislocation motions [22]. Only limited data were pertinent to the effect of interstitial atoms on the onset of yielding [6,23]. For example, interstitial hydrogen was recently found to reduce the critical load for incipient plasticity (or pop-in) during nanoindentation in FCC-NiCoCrFeMn [6,23]. On the other hand, interstitial carbon were found to increase the pop-in load during nanoindentation in an ultralow-carbon steel [24]. However, it has been shown that both interstitial hydrogen and carbon could enhance the tensile yield strength of their individual alloy matrices [24,25]. Apparently, the traditional wisdom that interstitial solute addition can lead to solid-solution hardening may not be applicable to the incipient plasticity measured by nanoindentation; the role of interstitial atoms on the incipient plasticity appears to be different. Therefore, it will be intriguing to differentiate the two processes and to identify their individual mechanisms. In this study, we employed instrumented nanoindentation, in combination with quantitative statistical analysis and density functional theory (DFT) calculations, to systematically examine the effect of interstitial oxygen and nitrogen additions on the incipient plasticity in BCC-NbTiZrHf HEAs, in an attempt to identify the origin for hardening during the incipient plasticity.

## 2. Methods

### 2.1. Experimental procedure

Ingots with nominal compositions of NbTiZrHf, (NbTiZrHf)<sub>98</sub>O<sub>2</sub> and (NbTiZrHf)<sub>98</sub>N<sub>2</sub> (at.%) were prepared by arc-melting a mixture of the constituent pure metals (purity > 99.9 wt.%), TiN (99.9 wt.%) and TiO<sub>2</sub> (99.9 wt.%) in an argon atmosphere purified by Ti-getter. The ingots were re-melted at least four times in high purity argon atmosphere to ensure chemical homogeneity before being drop-cast in a water-cooled copper mold. The as-cast ingots were then homogenized at 1290 °C for 24 h and cold rolled with 80% reduction in thickness. The rolled plates were additionally annealed at 1200 °C for 30 mins to remove the deformation substructure to obtain a recrystallized, equiaxed microstructure.

Phases and lattice parameter of each of the alloys were determined by synchrotron X-ray powder diffraction. Fine powders were ground from the annealed plates using an electric diamond grinding wheel saw. Synchrotron X-ray characterization was carried out at the 11-ID-B beamline with an X-ray wavelength of 0.2114 Å at the Advanced Photon Source at Argonne National Laboratory, USA. Microstructure and morphology of current alloys were characterized using a Zeiss Auriga scanning electron microscope (SEM) equipped with a Bruker QUANTAX electron backscatter diffraction (EBSD) system. Samples for EBSD examinations were prepared by initial mechanical polishing, followed by electrochemical polishing in a mixed solution of 6% perchloric acid + 30% n-butyl alcohol + 64% methyl at 30 V at room temperature. The dislocation structure beneath the indentation was taken using a Zeiss Libra 200 MC transmission electron microscopy (TEM) at an acceleration voltage of 200 kV. The cross-sectional thin foil of the indentation for TEM observation was prepared by Zeiss Auriga CrossBeam focused ion beam (FIB) system.

Instrumented nanoindentation experiments were conducted to investigate the pop-in behavior using a Berkovich diamond tip with an effective tip radius of ~270 nm in a Hysitron Triboindenter (Hysitron, Inc., USA) at room temperature. Indentations were

**Table 1**

Summary of lattice constants ( $a$ ), reduced moduli ( $E_r$ ), Young's moduli ( $E$ ), and shear moduli ( $G$ ) of NbTiZrHf and the interstitially alloyed HEAs.

Alloys	$a$ (Å)	$E_r$ (GPa)	$E$ (GPa)	$G$ (GPa)
Base HEA	3.4357	83.0	75.9	27.3
O-2 HEA	3.4376	88.1	80.9	29.1
N-2 HEA	3.4388	92.0	84.9	30.5

performed at a maximum load of 100 μN with a loading time of 10 s in load-controlled mode. Testes were made at a 5 μm interval to exclude possible overlap of the deformed zone produced by the adjacent indentations. Four grains were randomly selected and 121 nominally identical indentations on each grain were carried out to allow reliable statistical analysis of the pop-in behavior. To assess rate effect on pop-in behavior, various loading rates spanning two orders of magnitude (10–1000 μN/s) were applied. Additional nanoindentation hardness (deep indentation) tests were also performed at a high load of 8000 μN with various rates of 0.02, 0.1, 0.5, 2 s<sup>-1</sup>. The test samples for nanoindentation were prepared by electrochemical polishing mentioned above.

### 2.2. Computational methodology

First-principles DFT calculations were conducted to obtain the energetics and electronic structures of the present HEAs. The calculations were performed using the projector-augmented wave (PAW) method [26] as implemented in the Vienna ab initio Simulation Package (VASP) [27]. Special quasi-random structures (SQSs) supercell with 48 atoms was used to model the TiZrHfNb HEA which served as the base reference alloy state. Such SQSs were constructed to make the cluster correlations approach the expected value in a random atomic arrangement as closely as possible for a given structure size [28]. To investigate the effect of interstitial oxygen and nitrogen on the HEA, one interstitial atom of oxygen or nitrogen was inserted at the interstitial site (equivalent to 2 at.% concentration). In particular, both octahedral and tetrahedral interstitial sites that oxygen/nitrogen atom occupied were considered. All calculations were performed with spin-polarization and initialized in a ferromagnetic spin state. A reciprocal space discretization of 25 k-points per Å<sup>-1</sup> was applied, and the convergence criteria were set as 10<sup>-6</sup> eV for electronic loops.

## 3. Results

### 3.1. Microstructure characterization

Synchrotron high energy X-ray powder diffraction patterns of the annealed base HEA as well as the interstitially alloyed O-2 and N-2 HEAs are shown in Fig. 1a, which demonstrates that these samples have a single BCC crystal structure without any secondary phase, also confirming oxygen/nitrogen atoms are present as interstitials in the crystalline lattice. Based on the Rietveld method [29], the lattice parameters ( $a$ ) of the base, O-2, and N-2 HEAs are 3.4357 Å, 3.4376 Å, and 3.4388 Å, respectively; this is summarized in Fig. 1b and Table 1. Apparently, the presence of interstitial nitrogen or oxygen slightly increases the lattice parameter and the increment is larger for nitrogen than that for oxygen, which is probably associated with slightly larger atomic size of nitrogen.

Grain morphology and the corresponding size distribution in the annealed NbTiZrHf and interstitially alloyed HEAs characterized by EBSD are shown in Fig. 2, which reveals that current alloys consist of equiaxed grains with sizes varying in a wide range from 30 to 350 μm. Whereas NbTiZrHf has an average grain size of ~130 μm, the O-2 HEA has a slightly larger average grain size

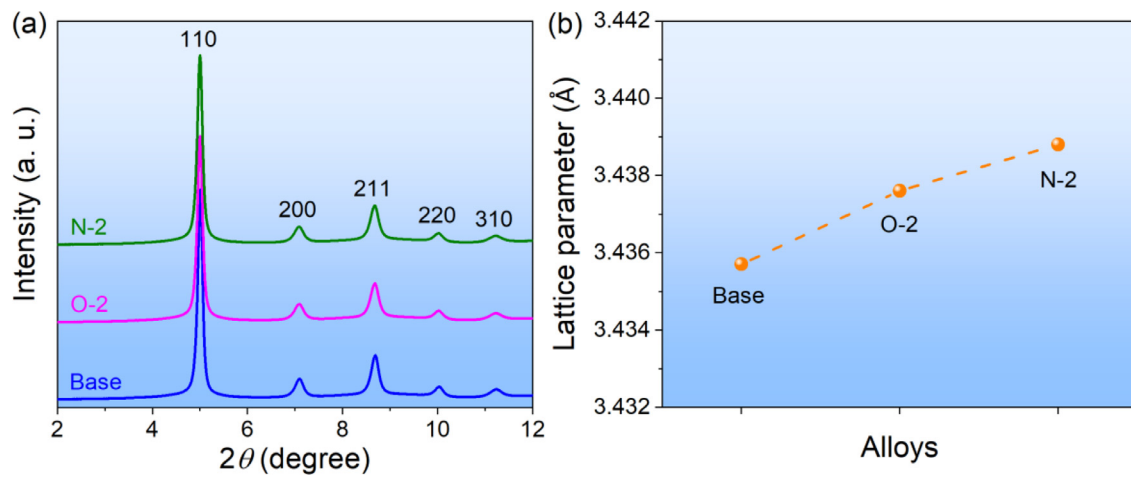


**Fig. 1.** (a) Synchrotron high energy X-ray powder diffraction patterns and (b) lattice parameters of the annealed equiatomic NbTiZrHf and interstitially alloyed HEAs.

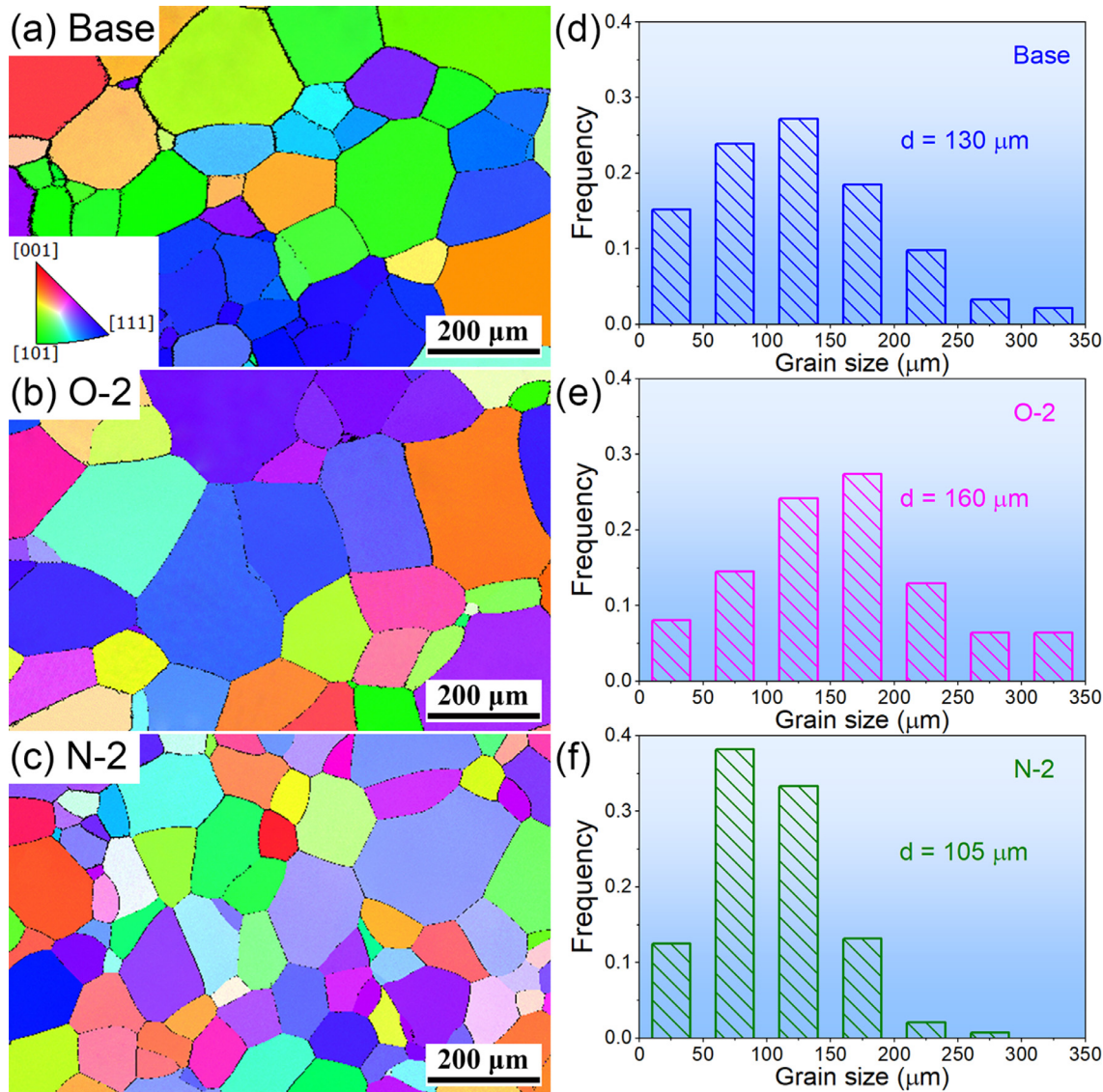


**Fig. 2.** (a-c) Electron back-scattering diffraction (EBSD) images, and (d-f) grain size distribution of the NbTiZrHf base, O-2, and N-2 HEAs, respectively.

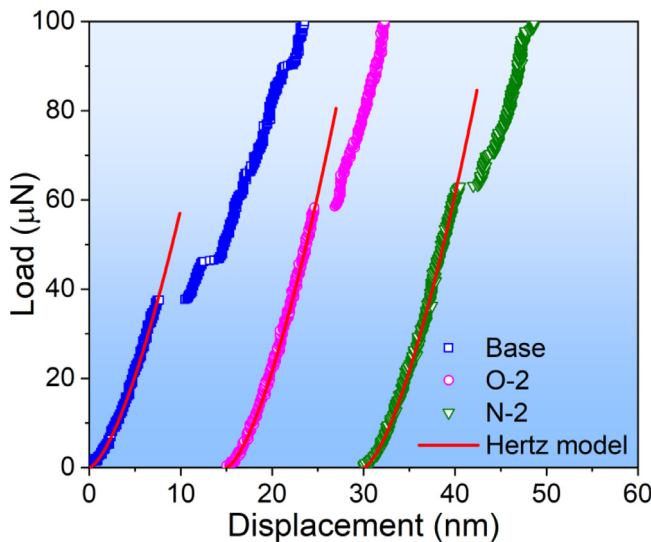


**Fig. 3.** Typical load-displacement curves at shallow indentation depth showing pop-in events of NbTiZrHf and interstitially alloyed HEAs.

of  $\sim 160 \mu\text{m}$  and the N-2 exhibits somewhat finer grain size of  $\sim 105 \mu\text{m}$ . This result indicates that the interstitial oxygen/nitrogen has only minor effect on the recrystallization and grain growth during annealing.

### 3.2. The first pop-in and maximum shear stress

Typical load-displacement (P-h) curves at shallow indentation for the base, O-2, and N-2 HEAs are shown in Fig. 3. For clarity, each curve is displaced along the x-axis and only the loading portion is presented. It is evident that the P-h curves for all three alloys exhibit “pop-ins”, i.e., displacement bursts. The first pop-in, which is indicative of the onset of yielding or incipient plasticity, occurs typically at a depth of  $\sim 10 \text{ nm}$ . Prior to the first pop-in, the initial portion of the load-displacement curves is the elastic response, can be described by Hertzian contact theory [30]

$$P = \frac{4}{3} E_r R^{1/2} h^{3/2} \quad (1)$$

where  $P$  is the applied indenting load,  $R$  the tip radius of indenter ( $\sim 270 \text{ nm}$ ),  $h$  the indentation depth,  $E_r$  the reduced elastic modulus

for a diamond indenter on HEA samples:

$$\frac{1}{E_r} = \frac{1 - \nu_i^2}{E_i} + \frac{1 - \nu_s^2}{E_s} \quad (2)$$

where  $\nu$  is Poisson's ratio,  $E$  is Young's modulus, and the subscripts  $i$  and  $s$  stand for properties of the diamond indenter and HEA samples. As shown in Fig. 3, the fitted red curves using the Hertz model agree well with the experimental results in the elastic region. It is noted that all P-h curves (2178 indentations in total) obtained in this study exhibit a clear pop-in, which appears to be affected by the presence of interstitial solutes. Specifically, as shown in Fig. 3, the critical load at the first pop-in in the interstitially alloyed HEAs are much higher than that in the interstitial-free base HEA, suggesting a solution hardening effect. Further discussion regarding this solution hardening in the pop-in load is in Section 4.

The reduced modulus can be readily derived from loading portion of the P-h curve according to Eq. (1). Statistical data collection of P-h<sup>3/2</sup> pairs at the first pop-in from 484 indentations in each alloy are presented in Fig. 4. As seen in the figure, the pop-in loads for NbTiZrHf are in the range of 25–50  $\mu\text{N}$ , but shift to much higher loads of 40–80  $\mu\text{N}$  for O-2 HEA and 45–90  $\mu\text{N}$  for N-2 HEA. The P-h<sup>3/2</sup> pairs can be well fitted by Eq. (1), as shown in Fig. 4, from which the reduced moduli ( $E_r$ ) can be readily deduced as 83.0, 88.1, and 92.0 GPa for NbTiZrHf, O-2, and N-2 HEAs, respectively. Insert the elastic parameters for diamond indenter ( $\nu_i = 0.07$  and  $E_i = 1141 \text{ GPa}$ ) and the HEA samples ( $\nu_s = 0.39$  [31]) into Eq. (2), the Young's moduli ( $E$ ) for the three materials are summarized in Table 1. Here, the Poisson's ratio of 0.39 for NbTiZrHf was measured using resonant ultrasound spectroscopy in a previous study [31] and the same value was used for the interstitially alloyed HEAs. Shear moduli ( $G$ ) were estimated using  $G = E/2(1 + \nu)$  and also included in Table 1. Evidently, the addition of oxygen or nitrogen to NbTiZrHf slightly increases the elastic moduli, and nitrogen has somewhat a larger effect than oxygen.

The maximum shear stress  $\tau_{max}$  at the first pop-in event can be estimated using Hertz's contact theory [30]:

$$\tau_{max} = \frac{0.47}{\pi} \left( \frac{4E_r}{3R} \right)^{2/3} P^{1/3} \quad (3)$$

where the maximum shear stress  $\tau_{max}$  is located at a depth of approximately 0.48 of the contact radius underneath the indenter tip. To statistically describe the stochastic characteristic of the first pop-ins, the cumulative probability distributions as a function of maximum shear stress for the present three HEAs are summarized in Fig. 5a. These distributions, the so-called nanoscale strength distributions (NSD), give the spread of measured strength

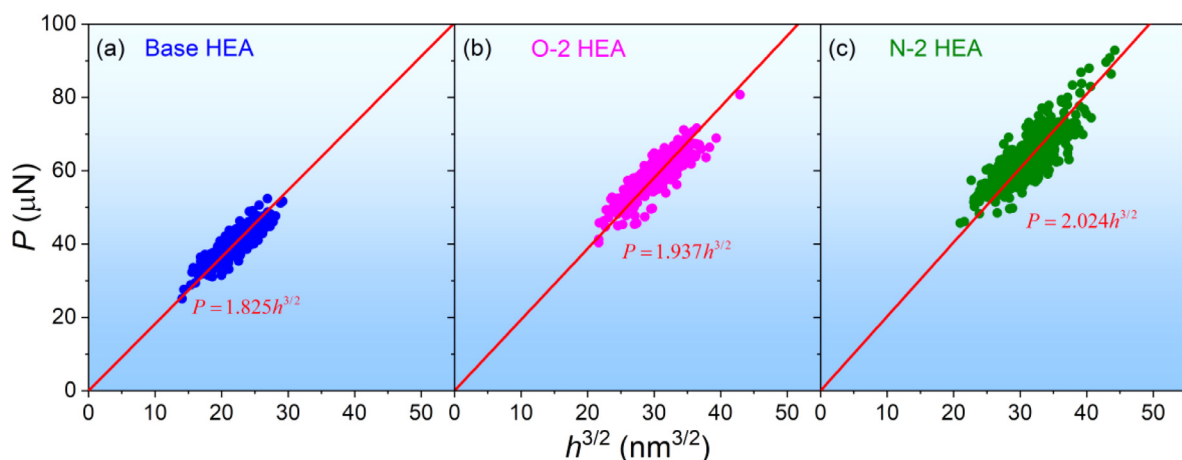


**Fig. 4.** Statistics of P-h<sup>3/2</sup> pairs at first pop-ins of NbTiZrHf and interstitially alloyed HEAs.

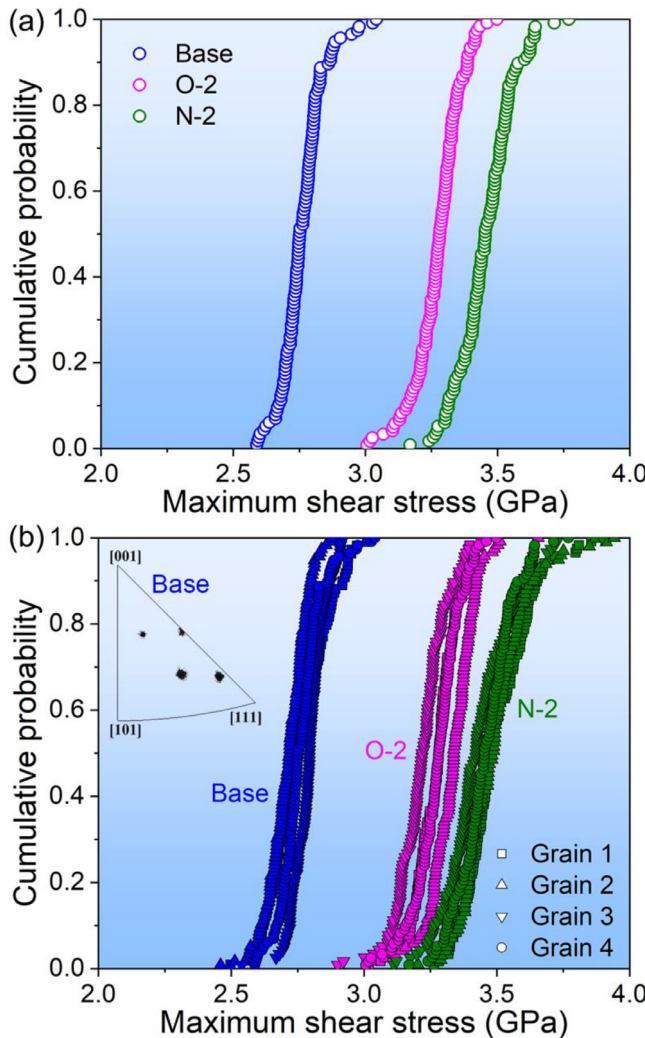


**Fig. 5.** (a) Cumulative probability of the first pop-in as a function of maximum shear stress of NbTiZrHf and interstitially alloyed HEAs. (b) A similar plot containing four grains for each alloy, with the upper left inset showing the corresponding orientations of the four grains for the NbTiZrHf HEA.

at which the maximum shear stress beneath the indenter that triggers the displacement bursts. It is readily observed that the cumulative probability curves for both interstitial-containing alloys shift towards higher stresses, and the shift is larger for the nitrogen-alloyed than that for the oxygen-alloyed sample. Specifically,  $\tau_{max}$  for NbTiZrHf is in the range of 2.5–3.1 GPa, while it varies in the ranges of 3.0–3.5 GPa and 3.1–3.8 GPa for O-2 and N-2 samples, respectively. The values of  $\tau_{max}$  are  $(1/11-1/9)G$  for NbTiZrHf and  $(1/10-1/8)G$  for the O-2 and N-2 samples, all of which approach the theoretical strength of  $\sim G/10$ , suggesting it is a result of dislocation nucleation. Extending the analysis to other grains, a similar plot of cumulative probability of the first pop-in for all selected grains is given in Fig. 5b. Although the O-2 HEA shows a slightly larger difference from grain to grain, NSD curves from four different grains almost overlap with each other for all HEAs, suggesting insignificant grain orientation dependence of the pop-in behavior in current HEAs. Similar observation has been reported in an FCC-NiCoCrFeMn HEA [5]. On the other hand, the addition of oxygen or nitrogen clearly increases the maximum shear stress for all grains, which reaffirms that the hardening effect on incipient plasticity has occurred because of interstitial alloying. Further discussion of the effect of interstitial solutes on the initiation of plasticity will be presented in Section 4.

### 3.3. Rate-dependent pop-in and activation volume

To evaluate the rate dependence of the dislocation nucleation process in the present interstitially alloyed HEAs, pop-in tests were performed at various loading rates, and the results are shown in Fig. 6a-c for NbTiZrHf, O-2, and N-2 HEAs, respectively. The NSD curves for the interstitially alloyed HEAs are always located at higher maximum shear stresses at any fixed loading rate. Also, the maximum shear stress required to trigger the pop-in is noted to increase with increasing loading rate for all three alloys, consistent with a stress-biased, thermally activated nucleation process [1,3]. In principle, a higher loading rate allows less time to initiate the pop-in event, thus lowers the probability to overcome the energy barrier by thermal fluctuations. Consequently, a higher shear stress is needed to nucleate dislocations. Similar results have been reported in several other metallic alloys, for example, FCC-NiCoCrFeMn HEA [5], BCC-Ti<sub>60</sub>(AlCrVNb)<sub>40</sub> MEA [32], BCC-Ta [8], FCC-Pt [1], and HCP-Mg [4].

To understand the underpinned atomic processes associated with the pop-in events, we conduct an analysis based on the transition-state theory combined with Weibull-type statistics proposed by Schuh et al. [1,3]. In this analysis, the cumulative probability  $F(P)$  is correlated with the indentation pop-in load  $P$  via the expression:

$$\ln[-\ln(1-F(P))] = \alpha P^{1/3} + \beta \quad (4)$$

where the parameter  $\beta$  is far weakly dependent on  $P$  as compared to the first term to the right-hand side [3]. The parameter  $\alpha$  is a collection of time-independent term, which can be correlated with the activation volume  $v^*$

$$v_{pop-in}^* = \frac{\pi}{0.47} \left( \frac{3R}{4E_r} \right)^{2/3} kT \cdot \alpha \quad (5)$$

In other words, the activation volume can be extracted from the slope  $\alpha$  in the  $\ln[-\ln(1-F)]$  vs.  $P^{1/3}$  plots (described in Eq. (4)), as shown in Fig. 6d-f for NbTiZrHf, interstitial-alloyed O-2 and N-2 HEAs, respectively. Following the above procedure, the average activation volumes are determined to be  $67 \text{ \AA}^3$  ( $3.3 \Omega$  or  $2.5 b^3$ ) for NbTiZrHf,  $54 \text{ \AA}^3$  ( $2.7 \Omega$  or  $2.0 b^3$ ) for O-2 HEA, and  $48 \text{ \AA}^3$  ( $2.4 \Omega$  or  $1.8 b^3$ ) for N-2 HEA. Here,  $\Omega$  is the atomic volume, and  $b$  is the Burger's vector. These activation volume values are tabulated in Table 2.

The activation volume is usually a good indicator to reveal the atomic process for dislocation nucleation [1–7]. For easy discussion, we also include activation volumes reported for a variety of conventional metals/alloys and HEAs [3–6,32–35] in Table 2. It is readily seen that the activation volume for well-annealed conventional pure metals and dilute alloys, irrespective of their crystal structures, is relatively small in the range of only  $0.3$ – $0.7 \Omega$ , suggesting it is associated with individual migration of point-like defect, such as vacancy and impurity. By contrast, the activation volume for well-annealed HEAs is much larger in the range of  $2$ – $4 \Omega$ , indicating that dislocation nucleation in HEAs involves cooperative migration of multiple atoms. One minor note on Table 2 is that the as-cast TiZrNbTa(Mo) HEAs and Ti<sub>60</sub>(AlCrVNb)<sub>40</sub> MEA exhibit lower activation volumes than the fully annealed ones. It is probably due to the fact that as-cast materials usually contain a higher population of defects (e.g., vacancy or dislocations), thus easier to facilitate dislocation nucleation. Also noted in Table 2 is that interstitial-alloying seems to have only a small effect on the activation volume. In fact, activation volume values are always at a magnitude of  $2$ – $3 \Omega$ , indicating a similar process governing dislocation nucleation in the present three HEAs.

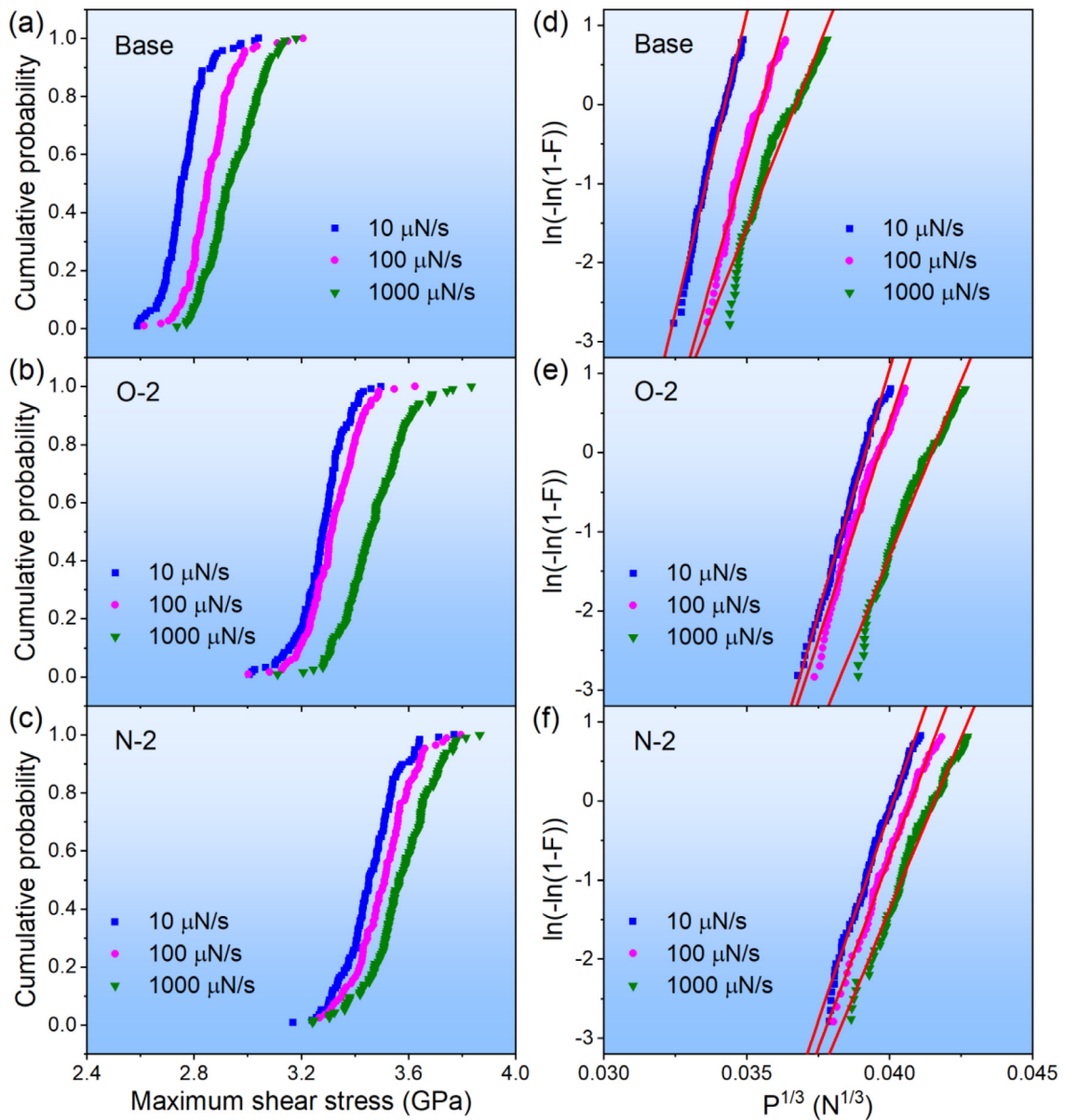


**Fig. 6.** (a-c) Nanoscale strength distributions (NSD) at various loading rates, and (d-f) the corresponding relation between  $\ln[\ln(1-F)^{-1}]$  and  $P^{1/3}$  of the NbTiZrHf base, O-2, and N-2 HEAs, respectively.

**Table 2**

Activation volume of dislocation nucleation characterized by nanoindentation pop-in tests in a variety of conventional metals/alloys and HEAs.

Materials	Material type	Processing	$v^*_{\text{pop-in}} (\Omega/b^3)$	References
Pt	FCC-pure metal	As-received	0.7/0.5	[3]
Ni	FCC-pure metal	Annealed	0.4/0.3	[33]
Cr	BCC-pure metal	Annealed	0.4/0.3	[34]
Mg	HCP-pure metal	Annealed	0.3–0.4/0.2–0.3	[4]
Mg-0.3 at.% X *	HCP-dilute alloys	Annealed	0.3–0.6/0.2–0.4	[4]
Ti <sub>60</sub> (AlCrVNb) <sub>40</sub>	BCC-MEA	As-cast	0.9/0.7	[32]
TiZrNbTa	BCC-HEA	As-cast	1.6/1.2	[35]
TiZrNbTaMo	BCC-HEA	As-cast	1.7/1.3	[35]
NiCoCrFeMn	FCC-HEA	Annealed	2.9/2.0	[5]
(NiCoCrFeMn) <sub>100-x</sub> H <sub>x</sub>	FCC-HEA	Homogenized	2–4/1.4–2.8	[6]
NbTiZrHf	BCC-HEA	Annealed	3.3/2.5	Present work
(NbTiZrHf) <sub>98</sub> O <sub>2</sub>	BCC-HEA	Annealed	2.7/2.0	Present work
(NbTiZrHf) <sub>98</sub> N <sub>2</sub>	BCC-HEA	Annealed	2.4/1.8	Present work

\* X = Al, Ca, Li, Y or Zn.

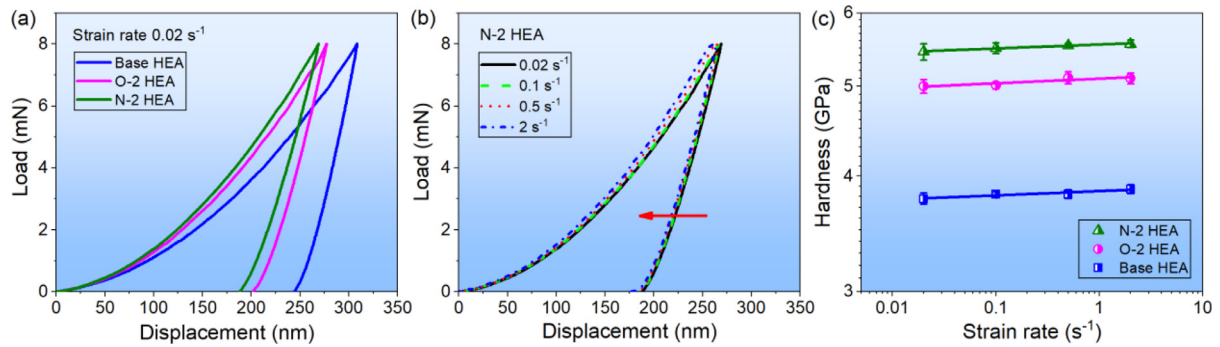


**Fig. 7.** (a) Representative load-displacement curves at deep indentation for present NbTiZrHf and interstitially alloyed HEAs at strain rate of  $0.02\text{ s}^{-1}$ . (b) Load-displacement curves for N-2 HEA at various strain rates. The direction of the red arrow represents the gradual increase in strain rate. (c) The double-log plot of nanoindentation hardness as a function of strain rate of present HEAs.

### 3.4. Differentiating mechanisms between pop-in and hardness

It is important to differentiate the kinetic processes between the indentation pop-in (yielding in a local dislocation-free crystalline region) and the conventional plastic yielding (global yielding in ordinary crystals containing dislocations). In the former, the process is controlled by dislocation nucleation (e.g., dislocation loop formation), whilst the latter is controlled by the locking and cutting/bypass of moving dislocation over obstacles. To separate them, we made efforts to examine the effect of interstitial solutes on hardness (deep indentation) and its rate-dependence to compare with that obtained from pop-in tests (shallow indentation). Representative load-displacement curves for NbTiZrHf and interstitially alloyed HEAs tested at deep indentation are given in Fig. 7a. At the fixed maximum load of 8 mN, NbTiZrHf exhibits the largest indentation depth (~300 nm), followed by O-2 and N-2 HEAs, showing considerable hardening effect due to the presence of interstitial oxygen and nitrogen ( $\Delta H_O = 0.41\text{ GPa}$  and  $\Delta H_N = 0.56\text{ GPa}$ ). Hardening during plastic deformation in metallic materials are generally associated with the interaction of dislocations with microstructural inhomogeneities, which leads to various mechanisms, such as solid-solution hardening, dislocation hardening, grain-boundary hardening, and precipitation hardening. In this study, all nanoindentation hardness tests were conducted within grain interiors (far away from grain boundaries) of well-annealed specimens, so grain-boundary hardening and dislocation hardening are safely excluded. Synchrotron high energy X-ray diffraction (Fig. 1) reveals the absence of secondary phase, which also rules out precipitation hardening. Consequently, interstitial solid-solution hardening appears to be the only possible mechanism for hardness enhancement in the O-2 or N-2 alloys. Apply the classical interstitial solid-solution strengthening model by Fleischer [11,36,37], specifically, tetragonal distortion generated by interstitial solutes in BCC lattice which inhibits dislocation motion, the increment in hardness  $\Delta H$  is estimated as

$$\Delta H = 3^{3/2} \frac{G \Delta \varepsilon c^{1/2}}{3} \quad (6)$$

where  $G$  is shear modulus (Table 1),  $\Delta \varepsilon$  denotes the difference between the longitudinal and transverse strain of the tetragonal distortion, and  $c$  (2% for both O-2 and N-2 HEAs) is the atomic concentration of interstitial atoms. By inserting appropriate parameters,  $\Delta \varepsilon$  values are calculated to be 0.17 and 0.22 for O-2 and N-2 HEAs, respectively. These  $\Delta \varepsilon$  values are comparable to those reported for other materials containing tetragonal distortions at room temperature [11,36–38], suggesting the occurrence of traditional interstitial solid-solution hardening.

To further investigate the rate dependence of hardness, load-displacement curves at various loading rates for the N-2 HEA are

**Table 3**

Activation volumes obtained from pop-in and hardness tests for NbTiZrHf and interstitially alloyed solid-solution HEAs.

Alloys	$v^*_{\text{pop-in}}$ ( $\text{\AA}^3/\Omega/b^3$ )	$v^*_{\text{hardness}}$ ( $\text{\AA}^3/\Omega/b^3$ )
Base HEA	67/3.3/2.5	1200/59.1/45.5
O-2 HEA	54/2.7/2.0	830/40.9/31.5
N-2 HEA	48/2.4/1.8	900/44.4/34.2

shown in Fig. 7b, in which the direction of the red arrow marks increasing strain rate. The indentation depth is noted to slightly decrease as the strain rate increases in the N-2 HEA specimens, indicative of increase in hardness. Curves obtained from NbTiZrHf and O-2 HEAs also follow a similar trend, but are not included here for brevity. Hardness of the three alloys as a function of strain rate is further plotted in a double-logarithmic graph in Fig. 7c, from which the strain rate sensitivity  $m$  is directly obtained from the slope. For a thermally activated deformation process, the strain rate sensitivity is linked to activation volume  $v^*$  via [39,40]

$$v^*_{\text{hardness}} = \frac{3\sqrt{3}kT}{mH} \quad (7)$$

where  $H$  is the hardness from nanoindentation tests,  $k$  and  $T$  have the same meaning as previously mentioned. The activation volumes for the present three HEAs are found to fall in the range of ~30–45  $b^3$ , as listed in Table 3. These values are in the typical range of 10–100  $b^3$ , indicating that deformation during hardness tests is probably similar to thermally activated kink-pair mechanism in coarse-grained BCC metals and alloys [41]. However, the activation volume obtained for pop-in is only approximately 2–3  $b^3$ , over one order of magnitude smaller than that obtained from the hardness tests. This distinct difference demonstrates that the mechanism for indentation pop-in, which is associated with the dislocation nucleation in a small, dislocation-free region beneath the indenter tip, is indeed quite different from that for hardness measurement, which involves interactions of moving dislocations with crystalline defects in a relatively large deformation volume. We may, therefore, conclude that strength enhancement during pop-in in the interstitially alloyed samples is not attributed to the classical interstitial solid-solution strengthening mechanism; other mechanism must prevail.

## 4. Discussion

Several mechanisms have been suggested to describe the effect of interstitials on the pop-in stress [6,24,42,43]. For example, it was found that the critical load at which the pop-in occurred during nanoindentation was much higher in the ultralow carbon steel than that in interstitial free steel [24]. It was argued that

the interstitial carbon atoms could lower the dislocation mobility and shorten the length of Frank-Read source for dislocation multiplication, so that a higher shear stress is necessary to activate the Frank-Read source according to  $\tau_{cr} = Gb/l_{cr}$ , where  $\tau_{cr}$  and  $l_{cr}$  are the critical shear stress and spacing of Frank-Read source, respectively. In other words, the model suggests pop-in is caused by a sudden multiplication of mobile dislocations. In our pop-in study, the indentation depth at which the pop-in occurred was shallow ( $h_c \sim 10$  nm), thus only a small volume of material was probed (estimated to be  $V \sim \pi a_c^3$  [3], where  $a_c = \sqrt{R h_c} \sim 50$  nm is the contact radius). Our previous TEM images taken from the annealed NbTiZrHf also revealed that dislocations were hardly observed prior to plastic deformation [16]. In addition, based on the fact the dislocation density is typically about  $10^6\text{--}10^8 \text{ cm}^{-2}$  in well-annealed metals and alloys [43,44], and the dislocation spacing would be about 1–10  $\mu\text{m}$ , which is far greater than the typical dimension of the stressed zone underneath the indenter ( $\sim 50$  nm). In such case, probability that the stressed zone underneath the fine indenter tip contains any pre-existing dislocation would be extremely low. Therefore, we may comfortably conclude that the pop-in stress is determined by dislocation nucleation, and dislocation multiplication from Frank-Read sources is not pertinent to our case.

Furthermore, the Frank-Read sources scenario is also difficult to reconcile with a recent observation that the presence of hydrogen in FCC NiCoCrFeMn HEA has significantly lowered the critical shear stress for the onset of yielding [6]. In this latter case, it was argued that hydrogen could induce the formation of stable hydrogen-vacancy complexes and increase vacancy concentration to promote the heterogeneous dislocation nucleation [45,46]. Since oxygen and nitrogen can also form their respective interstitial-vacancy complexes due to vacancy trapping [47–50], in a similar fashion, a reduced critical shear stress at pop-in is also expected to occur in our interstitials-containing HEAs. However, this expectation is obviously contrary to our results of having a higher pop-in load/stress. In fact, another recent atomistic molecular dynamics (MD) simulation study showed that hydrogen actually had no direct effect on dislocation nucleation during nanoindentation in Ni and Pd metals [42]. Therefore, it appears that there is no universal agreement on the effect of interstitials on the pop-in stress during nanoindentation. To clarify the exact role of interstitial oxygen/nitrogen on the pop-in stress in the current HEAs, we subsequently carry out the following DFT calculations.

Two types of slip systems are considered in the DFT calculations of ideal shear strength, i.e., the {110}<111> and {112}<111> shear deformations, as shown in Fig. 8. Affine shear deformation [51] is applied so that all the atoms in the simulation cell are deformed along the shear direction. The coordinate system of supercells is constructed with basis vectors of <1̄10>, <111> and <11̄2>, with <111> pointing in the slip direction.

The calculated energy as a function of shear strain for the {110}<111> and {112}<111> shears in the present NbTiZrHf and interstitially alloyed HEAs is shown in Fig. 9. The scenarios of oxygen/nitrogen atom in both octahedral and tetrahedral interstitial sites are particularly considered in the present study. The energy shows a sinusoidal-like evolution with the strain, and interstitials oxygen/nitrogen always increase the energy (N-2 > O-2 > base HEAs) for both interstitial sites under the two slip systems. The corresponding shear stress  $\tau$  can be obtained by differentiating the energy curves with respect to the strain  $\gamma$ , given by

$$\tau = \frac{1}{V} \frac{\partial U}{\partial \gamma} \quad (8)$$

where  $U$  and  $V$  are the energy and volume at a given strain, respectively. The maximum in the shear stress-strain curve is the ideal shear strength that a perfect crystal becomes unstable when

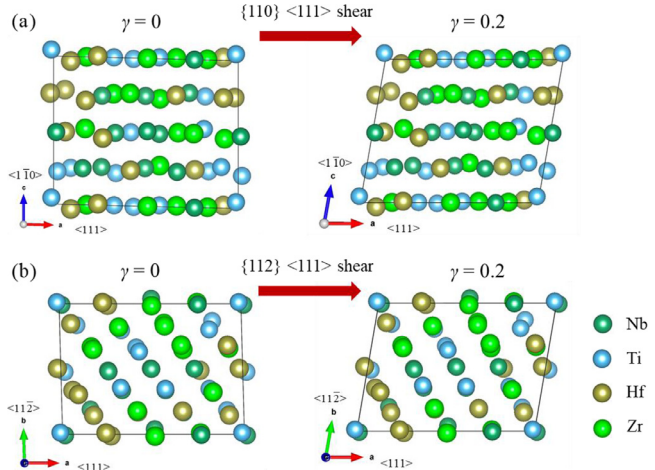


**Fig. 8.** Structures used for calculating the energy and stress of present HEAs under (a) {110}<111> and (b) {112}<111> shear deformations.

this stress is exceeded [52,53]. The shear stress-strain curves for both interstitial sites under both shear deformations are displayed in Fig. 10. Consistently, it can be readily observed that the impact of oxygen/nitrogen on shear stresses and energy follows the same trend, namely, N-2 > O-2 > base HEAs. It is worth noting that both energy and shear stress for the present HEAs under the {110}<111> shear deformation are much lower than those under {112}<111> shear, irrespective of octahedral or tetrahedral cases, indicating the {110}<111> shear is the easier shear path, thus the dominating slip system. To validate the DFT result, that is, the {110}<111> slip system dominates in the current HEAs, we further carried out TEM examination of dislocation activity after the pop-in. Representative post-mortem TEM images taken from the indentation with a depth of  $\sim 55$  nm for N-2 HEA are presented in Fig. 11. A large number of dislocations are observed underneath the indentation region in Fig. 11a and b, whereas the undeformed area that is far away from the indentation region presumably has very low dislocation density with essentially no contrast (not shown here). Neither phase transformation nor deformation twinning is detected underneath the indentation. As demonstrated in the selected area electron diffraction (SAED) patterns from two distant regions, i.e., away from the indentation (Fig. 11c) and beneath the indentation (Fig. 11d), only distorted diffraction spots presumably induced by deformation are developed after indentation. Dislocation patterns are revealed under two diffraction vectors, i.e.,  $\mathbf{g} = \bar{1}12$  (Fig. 11a) and  $\mathbf{g} = \bar{1}10$  (Fig. 11b). Based on the dislocation invisibility criterion, the  $\mathbf{g} = \bar{1}12$  reveals dislocations with Burges's vector of  $a/2$  [111] or  $a/2$  [11̄1], while  $\mathbf{g} = \bar{1}10$  indicates a Burges's vector of  $a/2$  [11̄1]. Furthermore, dislocations in Fig. 11a generally lie along the (110) plane, thus  $(\bar{1}10)[111]$  or  $(\bar{1}10)[11̄1]$  slip is identified. In summary, both TEM characterizations and DFT calculations consistently show that the incipient plasticity is primarily mediated by {110}<111> slip in present HEAs.

The above DFT calculations clearly reveal that interstitial oxygen/nitrogen can improve both energy and ideal shear strength of the NbTiZrHf HEA, and nitrogen produces a slightly larger effect than oxygen. This is consistent with the nanoindentation result, specifically, pop-in loads/stresses are, in an ascending order, NbTiZrHf < O-2 < N-2 HEAs (Figs. 3 and 5).

To further elucidate the origin of enhanced energy and ideal shear strength in oxygen/nitrogen alloyed HEAs, we analyze the local charge transfer between oxygen/nitrogen and metallic atoms in the first neighboring coordination shell. As the bader charge reflects the number of electrons localized near a certain atomic core [54,55], it can serve as a convenient tool to analyze the

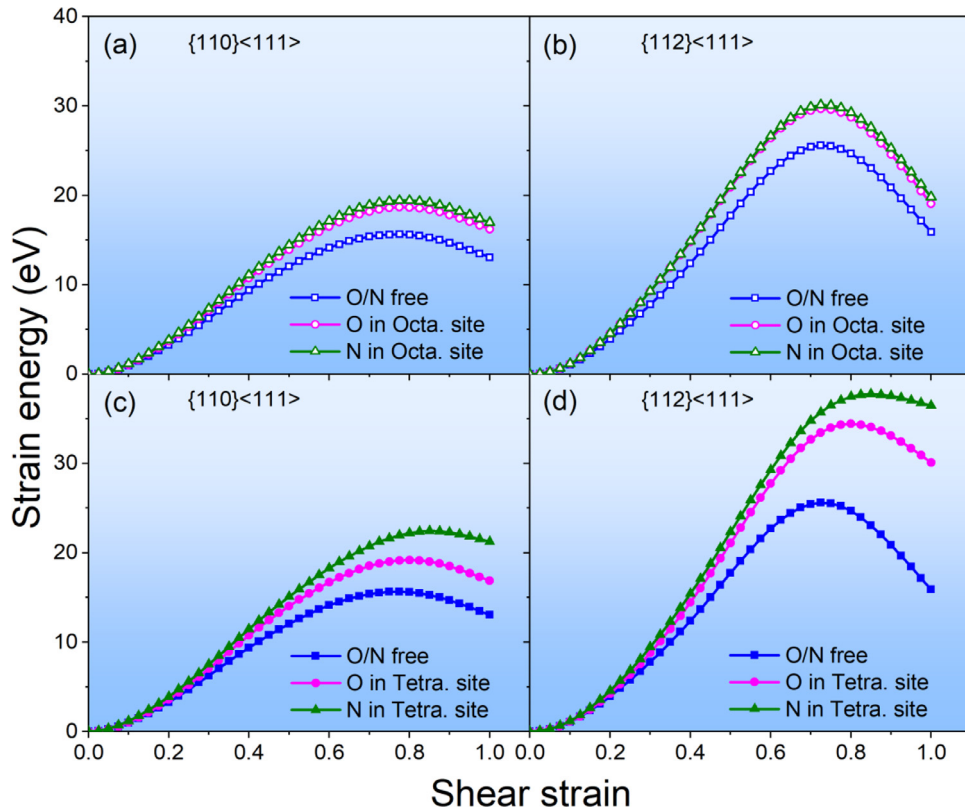


**Fig. 9.** Strain energy as a function of shear strain under  $\{110\}<111>$  (left column) and  $\{112\}<111>$  (right column) shear deformations for NbTiZrHf and interstitially alloyed HEAs considering oxygen/nitrogen atoms occupying octahedral (upper row) and tetrahedral (lower row) sites, respectively.

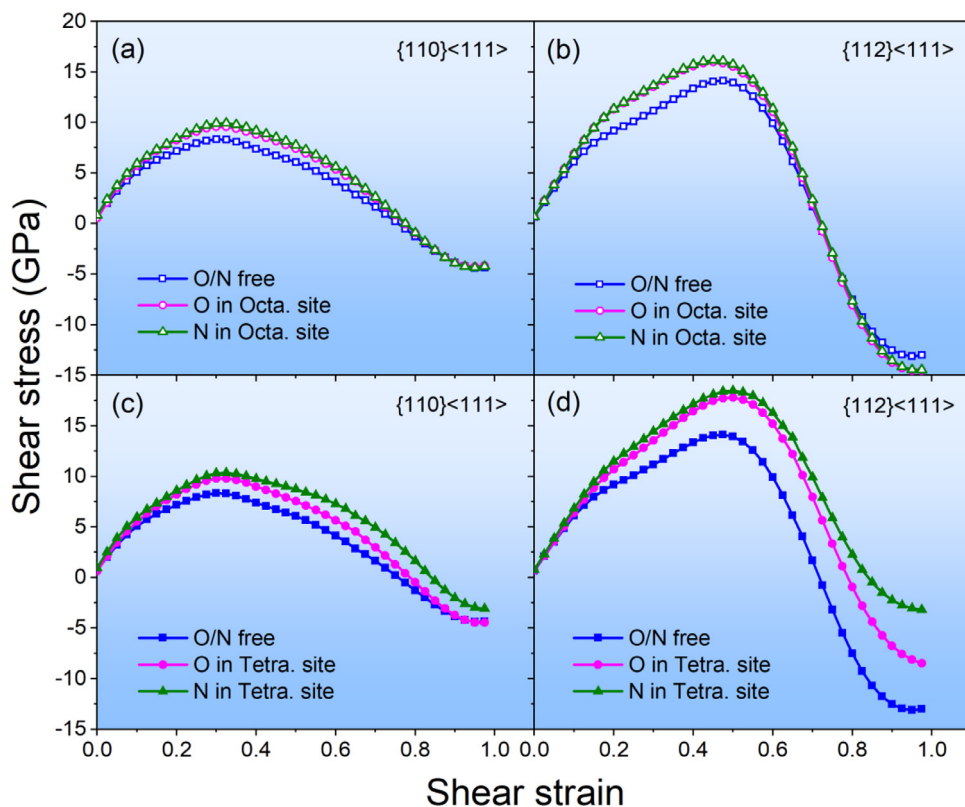


**Fig. 10.** Shear stress as a function of shear strain under  $\{110\}<111>$  (left column) and  $\{112\}<111>$  (right column) shear deformations for NbTiZrHf and interstitially alloyed HEAs considering oxygen/nitrogen atoms occupying octahedral (upper row) and tetrahedral (lower row) sites, respectively.

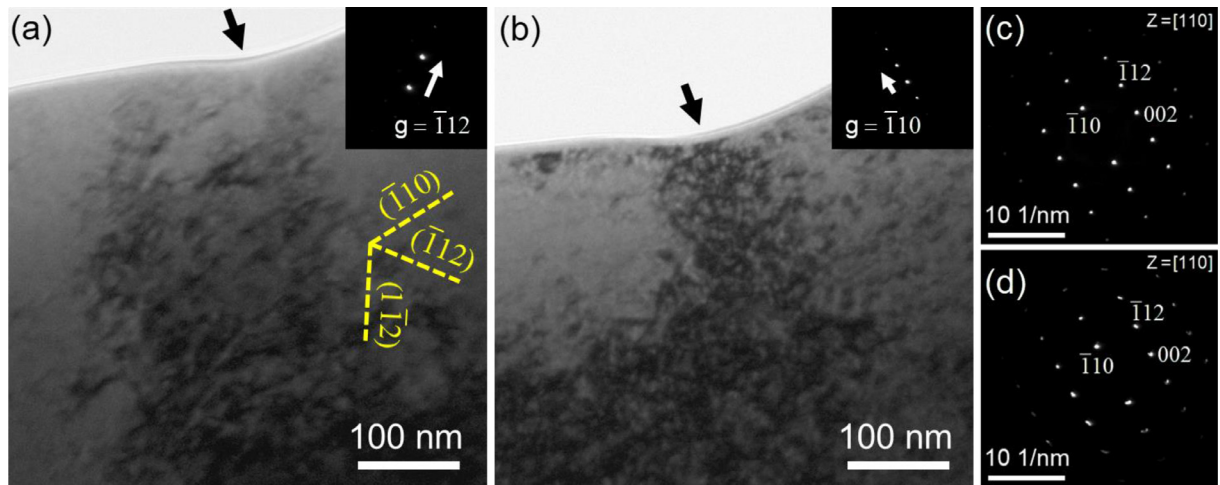


**Fig. 11.** Bright-field TEM images of N-2 HEA specimen showing the dislocation structure beneath the indentation observed under two-beam conditions with (a)  $\mathbf{g} = \bar{1}\bar{1}2$  and (b)  $\mathbf{g} = \bar{1}\bar{1}0$  diffraction vectors (white arrows in the insets). The black arrows denote the indentation direction, and yellow dash lines show the plane traces indicated. The corresponding SAED patterns along [110] zone axis taken from the regions: (c) away from the indentation and (d) underneath the indentation.

**Table 4**

Calculated bader charge for oxygen/nitrogen atom and its first neighboring coordination shell for octahedral and tetrahedral sites, respectively. The total valence electron considered in the DFT calculations is denoted as “total e<sup>-</sup>”.

Alloy system	O/N in octahedral site								O/N in tetrahedral site							
	Zr	Zr	Zr	Zr	Ti	Nb	O	N	Zr	Zr	Zr	Ti	O	N		
Total e <sup>-</sup>	12	12	12	12	10	11	6	5	12	12	12	10	6	5		
Base	11.7	11.77	11.79	11.78	9.3	11.89	/	/	11.77	11.79	11.78	9.3	/	/		
O-2	11.53	11.5	11.5	11.54	9.2	11.46	7.46	/	11.49	11.46	11.6	9.07	7.38	/		
N-2	11.6	11.39	11.42	11.43	9.02	11.41	/	6.75	11.39	11.42	11.43	9.01	/	6.75		

charge transfer among atoms. The calculated bader charge of oxygen/nitrogen and the surrounding metallic atoms for current three HEA systems are listed in Table 4. It is readily observed that the bader charges of metallic atoms for O-2 and N-2 HEAs are lowered when compared with that for the base HEA. On the other hand, oxygen or nitrogen atom attracts significant electrons from their local environment, which yields larger bader charge than their respective neutral state. Specifically, the bader charges of oxygen and nitrogen atoms increase by 1.46/1.38 e<sup>-</sup> and 1.75/1.75 e<sup>-</sup> for octahedral/tetrahedral sites, respectively. In other words, interstitials draw more charges from their nearest neighbor metal atoms in N-2 HEA than that in O-2 HEA. The charge transfer between oxygen/nitrogen and nearby metal atoms is anticipated to transform the original metal-metal bond to ionic-like metal-oxygen or metal-nitrogen bonds, which results in enhanced atomic cohesion. Such interstitial-metal matrix interaction can also be visualized in the plot of charge density isosurface in Fig. 12.

As a result of the enhanced cohesion, upon deformation, higher energy and stress are required to shear the metal-oxygen or metal-nitrogen bond in comparison with that in the interstitial-free alloy, as displayed in Figs. 9 and 10. A larger charge transfer in the N-2 HEA as compared to that in O-2 HEA certainly results in a higher energy and ideal shear strength. These calculations are all in line with the results obtained from nanoindentation pop-in experiments. It would be intriguing to estimate the number of the metal-oxygen or metal-nitrogen complexes ( $N_{\text{metal-O/N}}$ ) within the indented volume from the equation,

$$N_{\text{metal-O/N}} = \frac{\pi a_c^3 (\text{stressed volume})}{a^3 (\text{volume /unit cell})} \cdot 2 \\ (\text{atoms/unit cell}) \cdot 2\% (\text{O/N concentration}) \quad (9)$$

where  $a_c$  and  $a$  have the same meaning and values as previously mentioned,  $2(\pi a_c^3/a^3)$  includes all atom sites in the stressed vol-

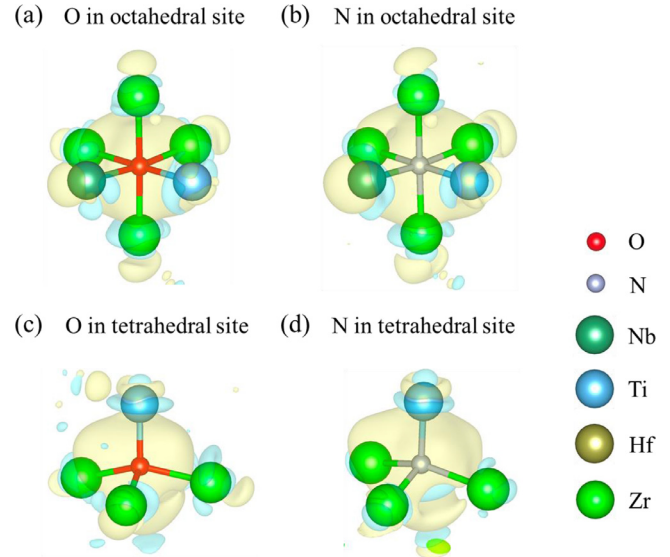


**Fig. 12.** Calculated 3D charge density plots illustrating the local bonding configurations for (a) oxygen in octahedral site, (b) nitrogen in octahedral site, (c) oxygen in tetrahedral site, and (d) nitrogen in tetrahedral site.

ume, and a uniform distribution of metal-oxygen/nitrogen complexes is assumed. In our case,  $N_{\text{metal-O/N}}$  is estimated to be of the order of  $10^5$  in the stressed volume. Obviously, such a large amount of metal-oxygen or metal-nitrogen complexes in the indented volume is expected to induce a notable effect on the dislocation nucleation in the present interstitially alloyed HEAs.

In summary, our DFT calculations reveal that improved pop-in stress in the current interstitial oxygen/nitrogen-containing HEAs

is not attributed to the modification of dislocation nucleation process, but rather associated with charge transfer between interstitials and their surrounding metallic atoms, which transforms metal-metal bond to ionic-like metal-oxygen or metal-nitrogen bonds with enhanced atomic cohesion.

## 5. Conclusions

We conducted a series of instrumented nanoindentation tests combined with quantitative statistical analysis and density functional theory (DFT) calculations to investigate the effect of interstitial oxygen and nitrogen on incipient plasticity and dislocation nucleation in well-annealed BCC-NbTiZrHf HEAs. Several key results and observations are summarized as follows.

- 1 The presence of interstitial oxygen and nitrogen atoms results in an increase in the pop-in load/stress at which dislocations are nucleated, and nitrogen has a slightly stronger hardening effect.
- 2 The maximum shear stress required to trigger dislocation nucleation is  $\sim 1/11$  to  $1/8$  of the shear modulus, approaching the respective theoretical strength. The observed indentation-induced incipient plasticity is predominantly mediated by the  $\{110\} <111>$  slip system in the currently studied BCC-HEAs.
- 3 The onset of yielding exhibits significant rate-dependence - a higher loading rate yields a higher pop-in load/stress. The activation volumes for dislocation nucleation (i.e., pop-in) in the present three HEAs are estimated to be  $\sim 1.8\text{--}2.5 b^3$ , corresponding to 2–3 atomic volumes, indicating the nucleation process involves cooperative migration of multiple constituent atoms. In comparison, the activation volumes obtained from deep indentation in hardness test are much larger at  $\sim 30\text{--}45 b^3$ , implying a different dislocation process dominated by thermally activated kink-pair mechanism. In this case, hardness enhanced by interstitial oxygen or nitrogen is a result of the traditional interstitial solid-solution strengthening, i.e., dislocation moving through a crystalline lattice distorted by interstitials.
- 4 The first-principles calculations reveal that the interstitial (oxygen/nitrogen) and its surrounding neighboring metals form metal-interstitial complexes with strong ionicity resulting from significant charge transfer. These complexes have a strong atomic cohesion between the interstitial and its neighboring metals, thus requires higher energy and stress to initiate shear deformation. It offers an explanation for the observed increase in the critical shear stress necessary for dislocation nucleation in the current interstitials-containing HEAs.

## Declaration of Competing Interest

The authors declare that they have no known competing financial interests or personal relationships that could have appeared to influence the work reported in this paper.

## Acknowledgement

This work was supported by the National Science Foundation under Contract NSF DMR-1408722. Y.X.Ye would also like to acknowledge funding from the State of Tennessee and Tennessee Higher Education Commission (THEC) through their support of the Center for Materials Processing (CMP). We would like to thank Dr. Yang Tong at ORNL for helping the synchrotron XRD, Prof. Zhaoping Lu at USTB for providing test samples, and Prof. Haixuan Xu at UTK and Prof. Xiongjun Liu at USTB for technical discussion and suggestions on DFT calculations.

## References

- [1] C.A. Schuh, J.K. Mason, A.C. Lund, Quantitative insight into dislocation nucleation from high-temperature nanoindentation experiments, *Nat Mater* 4 (2005) 617–621.
- [2] C.A. Schuh, A.C. Lund, Application of nucleation theory to the rate dependence of incipient plasticity during nanoindentation, *J Mater Res* 19 (2004) 2152–2158.
- [3] J.K. Mason, A.C. Lund, C.A. Schuh, Determining the activation energy and volume for the onset of plasticity during nanoindentation, *Physical Review B* 73 (2006) 054102.
- [4] H. Somekawa, C.A. Schuh, Effect of solid solution elements on nanoindentation hardness, rate dependence, and incipient plasticity in fine grained magnesium alloys, *Acta Mater* 59 (2011) 7554–7563.
- [5] C. Zhu, Z.P. Lu, T.G. Nieh, Incipient plasticity and dislocation nucleation of Fe-CoCrNiMn high-entropy alloy, *Acta Mater* 61 (2013) 2993–3001.
- [6] G. Yang, Y. Zhao, D.-H. Lee, J.-M. Park, M.-Y. Seok, J.-Y. Suh, U. Ramamurty, J.-I. Jang, Influence of hydrogen on incipient plasticity in CoCrFeMnNi high-entropy alloy, *Scr Mater* 161 (2019) 23–27.
- [7] Y.X. Ye, Z.P. Lu, T.G. Nieh, Dislocation nucleation during nanoindentation in a body-centered cubic TiZrHfNb high-entropy alloy, *Scr Mater* 130 (2017) 64–68.
- [8] M.M. Biener, J. Biener, A.M. Hodge, A.V. Hamza, Dislocation nucleation in bcc Ta single crystals studied by nanoindentation, *Physical Review B* 76 (2007) 165422.
- [9] J.R. Morris, H. Bei, G.M. Pharr, E.P. George, Size effects and stochastic behavior of nanoindentation pop in, *Phys. Rev. Lett.* 106 (2011) 165502.
- [10] S. Shim, H. Bei, E.P. George, G.M. Pharr, A different type of indentation size effect, *Scr Mater* 59 (2008) 1095–1098.
- [11] Z. Lei, X. Liu, Y. Wu, H. Wang, S. Jiang, S. Wang, X. Hui, Y. Wu, B. Gault, P. Kontis, D. Raabe, L. Gu, Q. Zhang, H. Chen, H. Wang, J. Liu, K. An, Q. Zeng, T.-G. Nieh, Z. Lu, Enhanced strength and ductility in a high-entropy alloy via ordered oxygen complexes, *Nature* 563 (2018) 546–550.
- [12] T. Yang, Y. Zhao, Y. Tong, Z. Jiao, J. Wei, J. Cai, X. Han, D. Chen, A. Hu, J. Kai, Multicomponent intermetallic nanoparticles and superb mechanical behaviors of complex alloys, *Science* 362 (2018) 933–937.
- [13] Z. Li, K.G. Pradeep, Y. Deng, D. Raabe, C.C. Tasan, Metastable high-entropy dual-phase alloys overcome the strength-ductility trade-off, *Nature* 534 (2016) 227–230.
- [14] B. Gludovatz, A. Hohenwarter, D. Catoor, E.H. Chang, E.P. George, R.O. Ritchie, A fracture-resistant high-entropy alloy for cryogenic applications, *Science* 345 (2014) 1153–1158.
- [15] D.-H. Lee, M.-Y. Seok, Y. Zhao, I.-C. Choi, J. He, Z. Lu, J.-Y. Suh, U. Ramamurty, M. Kawasaki, T.G. Langdon, Spherical nanoindentation creep behavior of nanocrystalline and coarse-grained CoCrFeMnNi high-entropy alloys, *Acta Mater* 109 (2016) 314–322.
- [16] Y.X. Ye, C.Z. Liu, H. Wang, T.G. Nieh, Friction and wear behavior of a single-phase equiatomic TiZrHfNb high-entropy alloy studied using a nanoscratch technique, *Acta Mater* 147 (2018) 78–89.
- [17] Y.Y. Zhao, Y.X. Ye, C.Z. Liu, R. Feng, K.F. Yao, T.G. Nieh, Tribological behavior of an amorphous Zr20Ti20Cu20Ni20Be20 high-entropy alloy studied using a nanoscratch technique, *Intermetallics* 113 (2019) 106561.
- [18] Z. Wang, I. Baker, Z. Cai, S. Chen, J.D. Poplawsky, W. Guo, The effect of interstitial carbon on the mechanical properties and dislocation substructure evolution in Fe40.4Ni11.3Mn34.8Al7.5Cr6 high entropy alloys, *Acta Mater* 120 (2016) 228–239.
- [19] I. Moravcik, H. Hadra, L. Li, I. Dlouhy, D. Raabe, Z. Li, Yield strength increase of a CoCrNi medium entropy alloy by interstitial nitrogen doping at maintained ductility, *Scr Mater* 178 (2020) 391–397.
- [20] J.B. Seol, J.W. Bae, Z. Li, J.C. Han, J.G. Kim, D. Raabe, H.S. Kim, Boron doped ultrastrong and ductile high-entropy alloys, *Acta Mater* 151 (2018) 366–376.
- [21] P.-J. Yang, Q.-J. Li, T. Tsuru, S. Ogata, J.-W. Zhang, H.-W. Sheng, Z.-W. Shan, G. Sha, W.-Z. Han, J. Li, Mechanism of hardening and damage initiation in oxygen embrittlement of body-centred-cubic niobium, *Acta Mater* 168 (2019) 331–342.
- [22] T.H. Courtney, *Mechanical Behaviour of Materials*, 2nd ed., Waveland Press, Long Grove, 2005.
- [23] D. Wang, X. Lu, Y. Deng, D. Wan, Z. Li, A. Barnoush, Effect of hydrogen-induced surface steps on the nanomechanical behavior of a CoCrFeMnNi high-entropy alloy revealed by in-situ electrochemical nanoindentation, *Intermetallics* 114 (2019) 106605.
- [24] K. Sekido, T. Ohmura, L. Zhang, T. Hara, K. Tsuzaki, The effect of interstitial carbon on the initiation of plastic deformation of steels, *Materials Science and Engineering: A* 530 (2011) 396–401.
- [25] H. Luo, Z. Li, D. Raabe, Hydrogen enhances strength and ductility of an equiatomic high-entropy alloy, *Sci Rep* 7 (2017) 1–7.
- [26] G. Kresse, D. Joubert, From ultrasoft pseudopotentials to the projector augmented-wave method, *Physical Review B* 59 (1999) 1758.
- [27] G. Kresse, J. Furthmüller, Efficiency of ab-initio total energy calculations for metals and semiconductors using a plane-wave basis set, *Computational Materials Science* 6 (1996) 15–50.
- [28] A. Zunger, S.-H. Wei, L. Ferreira, J.E. Bernard, Special quasirandom structures, *Phys. Rev. Lett.* 65 (1990) 353.
- [29] R.A. Young, *The Rietveld Method*, Oxford University Press, 1993.
- [30] K.L. Johnson, *Contact Mechanics*, Cambridge University Press, Cambridge, 1987.

- [31] Y.X. Ye, B.L. Musico, Z.Z. Lu, L.B. Xu, Z.F. Lei, V. Keppens, H.X. Xu, T.G. Nieh, Evaluating elastic properties of a body-centered cubic NbHfZrTi high-entropy alloy – A direct comparison between experiments and ab initio calculations, *Intermetallics* 109 (2019) 167–173.
- [32] X.K. Zhang, J.C. Huang, P.H. Lin, W.S. Chuang, T.Y. Liu, Y.C. Wu, Y.C. Liao, J.S.C. Jang, Effect of orientation and loading rate on the incipient behavior of Ti<sub>60</sub>(AlCrVNb)<sub>40</sub> medium entropy alloy, *Materials Science and Engineering: A* 775 (2020) 138969.
- [33] S. Mridha, M. Sadeghilardjani, S. Mukherjee, Activation volume and energy for dislocation nucleation in multi-principal element alloys, *Metals (Basel)* 9 (2019) 263.
- [34] D. Wu, T.G. Nieh, Incipient plasticity and dislocation nucleation in body-centered cubic chromium, *Materials Science and Engineering: A* 609 (2014) 110–115.
- [35] S.-P. Wang, J. Xu, Incipient plasticity and activation volume of dislocation nucleation for TiZrNbTaMo high-entropy alloys characterized by nanoindentation, *Journal of Materials Science & Technology* 35 (2019) 812–816.
- [36] R.L. Fleischer, Rapid solution hardening, dislocation mobility, and the flow stress of crystals, *J Appl Phys* 33 (1962) 3504–3508.
- [37] T. Mitchell, A. Heuer, Solution hardening by aliovalent cations in ionic crystals, *Materials Science and Engineering* 28 (1977) 81–97.
- [38] A. Cochardt, G. Schoek, H. Wiedersich, Interaction between dislocations and interstitial atoms in body-centered cubic metals, *Acta Metallurgica* 3 (1955) 533–537.
- [39] Q. Wei, Z. Pan, X. Wu, B. Schuster, L. Kecskes, R. Valiev, Microstructure and mechanical properties at different length scales and strain rates of nanocrystalline tantalum produced by high-pressure torsion, *Acta Mater* 59 (2011) 2423–2436.
- [40] D. Wu, X. Wang, T. Nieh, Variation of strain rate sensitivity with grain size in Cr and other body-centred cubic metals, *J Phys D Appl Phys* 47 (2014) 175303.
- [41] V. Maier-Kiener, B. Schuh, E.P. George, H. Clemens, A. Hohenwarter, Insights into the deformation behavior of the CrMnFeCoNi high-entropy alloy revealed by elevated temperature nanoindentation, *J Mater Res* 32 (2017) 2658–2667.
- [42] X. Zhou, B. Ouyang, W. Curtin, J. Song, Atomistic investigation of the influence of hydrogen on dislocation nucleation during nanoindentation in Ni and Pd, *Acta Mater* 116 (2016) 364–369.
- [43] K. Nibur, D. Bahr, B. Somerday, Hydrogen effects on dislocation activity in austenitic stainless steel, *Acta Mater* 54 (2006) 2677–2684.
- [44] G.K. Williamson, R.E. Smallman III, Dislocation densities in some annealed and cold-worked metals from measurements on the X-ray debye-scherrer spectrum, *Philosophical Magazine* 1 (1956) 34–46.
- [45] I. Salehinia, V. Perez, D. Bahr, Effect of vacancies on incipient plasticity during contact loading, *Philosophical Magazine* 92 (2012) 550–570.
- [46] E. Njeim, D. Bahr, Atomistic simulations of nanoindentation in the presence of vacancies, *Scr Mater* 62 (2010) 598–601.
- [47] C. Domain, C. Becquart, J. Focet, Ab initio study of foreign interstitial atom (C, N) interactions with intrinsic point defects in  $\alpha$ -Fe, *Physical Review B* 69 (2004) 144112.
- [48] M. Wu, X. Liu, J. Gu, Z. Jin, DFT study of nitrogen–vacancy complexions in (fcc) Fe, *Modelling and Simulation in Materials Science and Engineering* 22 (2014) 055004.
- [49] H. Zenia, K. Lounis, E. Megchiche, C. Mijoule, Stability of vacancy–oxygen complexes in bulk nickel: atomistic and ab initio calculations, *Computational Materials Science* 124 (2016) 428–437.
- [50] M. Pesola, J. Von Boehm, T. Mattila, R.M. Nieminen, Computational study of interstitial oxygen and vacancy–oxygen complexes in silicon, *Physical Review B* 60 (1999) 11449.
- [51] L. Casillas-Trujillo, L. Xu, H. Xu, Compositional effects on ideal shear strength in Fe-Cr alloys, *J Alloys Compd* 720 (2017) 466–472.
- [52] D. Roundy, C. Krenn, M.L. Cohen, J. Morris Jr., Ideal shear strengths of fcc aluminum and copper, *Phys. Rev. Lett.* 82 (1999) 2713.
- [53] W. Luo, D. Roundy, M.L. Cohen, J. Morris Jr., Ideal strength of bcc molybdenum and niobium, *Physical Review B* 66 (2002) 094110.
- [54] G. Henkelman, A. Arnaldsson, H. Jónsson, A fast and robust algorithm for Bader decomposition of charge density, *Computational Materials Science* 36 (2006) 354–360.
- [55] E. Sanville, S.D. Kenny, R. Smith, G. Henkelman, Improved grid-based algorithm for Bader charge allocation, *J Comput Chem* 28 (2007) 899–908.